# Wave mode separation and prestack depth migration of multicomponent data in the presence of topography

Saul E. Guevara* and Gary F. Margrave †

## ABSTRACT

Scalar methods for multicomponent data processing require in principle separate wave modes. A method for wave mode separation in the presence of topography is proposed and tested on synthetic seismic data, generated over a complex geology model with a 2D elastic FD method. The resulting data are migrated using two preSDM approaches, Kirchhoff and PSPI, which also take into account the rough topography. The seismic images obtained show the challenging characteristics of these data; the methods provide insights into approaches that can be rewarding for elastic wave processing in complex settings.

## INTRODUCTION

In current practice, processing of $P$ and $S$ wave data in multicomponent technology is carried out by one-component scalar methods, which require separated wave-modes. It is usually assumed that the vertical component signal corresponds to $P$-wave, and the horizontal one to $S$-wave, which is a reasonable approximation for approximately flat settings with a low velocity Near-Surface (NS) layer. However complex areas can include rock outcrops with high velocity, rough topography, and NS heterogeneity over short distance. These properties may have a significant effect on reflections from depth interfaces at depth, and violate the flat surface normal incidence assumptions.

Potential advantages have been identified in methods for wave-mode separation of multicomponent data (see e.g. Van der Baan, 2006). A method taking into account that a seismic wave recorded at the free surface is the result of the interaction between the incident wave, propagated through the body of the medium, and the free surface, was proposed by Dankbaar (1985). Its application to a setting with rough topography is investigated in this work.

On the other hand Prestack Depth Migration (preSDM) is considered the most appropriate imaging method in complex areas (Gray et al., 2001). It usually assumes a flat surface, which simplifies processing and interpretation. However, this method can be insufficient in the case of complex areas, with rough topography. These shortcomings have encouraged the investigation into methods that better honor wave equation propagation laws, such as migration from surface (Gray and Marfurt, 1995), without a flat datum assumption. An investigation into preSDM from a rough surface, applied to multicomponent data is presented in this report.

*University of Calgary
†Devon Energy

First, a wave mode separation method, taking into account the free surface effect in the presence of rough topography, is presented. Next, two preSDM methods from topography, each a different approach, are introduced. A synthetic multicomponent 2D data set, generated from a geological model with topography and complex structure, illustrates these methods. Work on the same topics have been presented previously in CREWES Reports (Guevara and Margrave, 2011; Guevara et al., 2013). In this work, the methods have been extended, more accurately defined and applied to a common data set.

## THEORETICAL PRINCIPLES

### The free surface effect and wave mode separation with topography

*The free surface effect*

Reflection data recorded at the free surface do not correspond to a body wave traveling through the medium, since reflections and wave mode conversions are generated at the free surface, and the images on both vertical and horizontal components results from this interaction. This phenomenon is known as the *free-surface effect*, which depends on the angle of incidence and the elastic properties of the near-surface (e.g. Meissner, 1965). The relation between the incident $P$ and $S$-waves and the recorded $x$ and $z$ components is expressed as the free-surface response coefficients, obtained from the boundary condition of no stress at the free surface, and assuming an incident plane wave, which can be represented by its horizontal slowness $p$. Thereby, according to Dankbaar (1985), the free surface response coefficients $R^{\chi}_{\varrho}$ as a function of the slowness $p$ and the NS velocities $V_P$ and $V_S$ are:

$$R^z_P(p) = 2\,V_P/V_S\,\left((V_S/V_P)^2 - V_S^2\,p^2\right)^{1/2}\,(2V_S^2\,p^2 - 1)/R_0(p) \tag{1a}$$

$$R^z_S(p) = 4\,V_S\,p\,\left((V_S/V_P)^2 - V_S^2\,p^2\right)^{1/2}\,(1 - V_S^2\,p^2)^{1/2}/R_0(p) \tag{1b}$$

$$R^x_P(p) = 4\,V_P\,p\,\left((V_S/V_P)^2 - V_S^2\,p^2\right)^{1/2}\,(1 - V_S^2\,p^2)^{1/2}/R_0(p) \tag{1c}$$

$$R^x_S(p) = 2\,(1 - V_S^2\,p^2)^{1/2}\,(1 - 2V_S^2\,p^2)/R_0(p) \tag{1d}$$

The $R^{\chi}_{\varrho}$ subscript $\varrho$ indicates the wave modes, $P$ or $S$, and the superscript $\chi$ is the components direction, $x$ or $z$. The denominator is:

$$R_0(p) = (1 - 2V_S^2\,p^2)^2 + 4\,p^2V_S^2\,\left((V_S/V_P)^2 - V_S^2\,p^2\right)^{1/2}\,(1 - V_S^2\,p^2)^{1/2}$$

Figure 1 illustrates the wave mode decomposition at the free surface to obtain these coefficients. Figure 2 shows an example of these coefficients as a function of the angle of incidence for an $S$-wave, assuming a velocity model of $V_P$ 2000 and $V_S$ 1000 m/s.

*Wave mode separation in the $Tau$-$p$ domain*

Since these coefficients are a function of the angle of incidence of a plane wave, they could be applied to a wave field decomposed into plane waves. It can be obtained through the $Tau$-$p$ transform, as shown by Donati (1996), which is defined as:

$$RT\,[u(t,x)] = \hat{u}(\tau,p) = \int_{-\infty}^{\infty} u(\tau + px, x)\mathrm{d}x \quad , \tag{2}$$

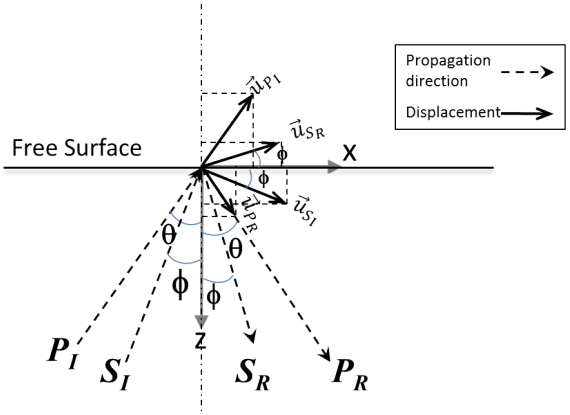


FIG. 1. Free-surface effect: decomposition of $P$ and $S$ waves arriving at the surface, for incident $P$-wave ($P_I$), and $S$ wave ($S_I$). Coordinate axes are $x$ increasing to the right and $z$ increasing downward. $P_R$ identifies the reflected $P$-wave, and $S_R$ the reflected $S$-wave. The displacements are identified by the vector $\vec{u}$, with a subindex for each type of wave.

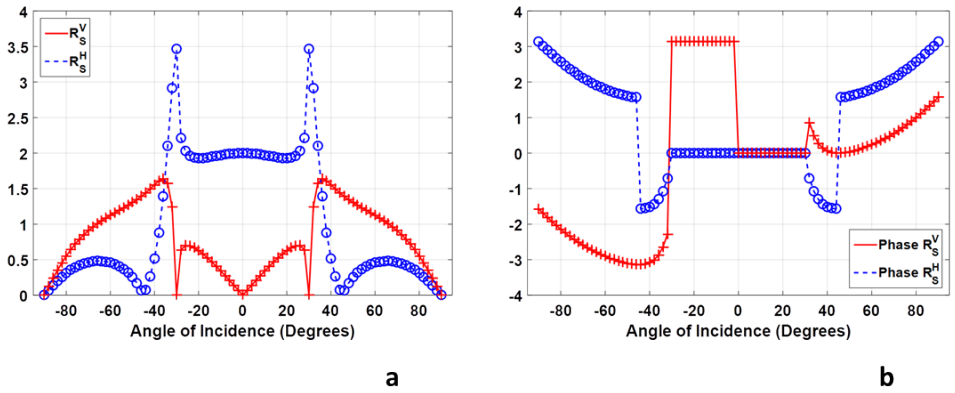


FIG. 2. Example of the free-surface effect as a function of the angle of incidence for $S$-wave arrival. $V_P$ 2000 m/s and $V_S$ is 1000 m/s. (a) Amplitude response, (b) Phase response. Red is the vertical component and blue the horizontal one.

where $u(t,x)$ is a seismic data record in time and space, and the transformed $\hat{u}(\tau,p)$ stands for the data in intercept time ($\tau$)-ray parameter ($p$) domain (Margrave, 2007).

The discrete $Tau$-$p$ transform can be obtained in the frequency domain. Following Marfurt et al. (1996), the discrete inverse $Tau$-$p$ transform is:

$$u(\omega,x) = \underset{\sim}{\mathcal{T}}(\omega,p,x)\hat{u}(\omega,p) \tag{3}$$

$\underset{\sim}{\mathcal{T}}$ is a matrix operator with discrete elements defined by

$$T_{jk} = e^{i\omega p_j x_k} \quad ,$$

such that equation 3 can also be represented in discrete shape as:

$$u_k = \sum_{j=1}^{n_p} e^{i\omega p_j x_k}\hat{u}_j \quad . \tag{4}$$

The $Tau$-$p$ transform can be obtained by least squares inversion according to:

$$\hat{u}(\omega,p) = \left[\underset{\sim}{\mathcal{T}}^H\underset{\sim}{\mathcal{T}}\right]^{-1}\underset{\sim}{\mathcal{T}}^H u(\omega,x) \quad , \tag{5}$$

where the exponent $^H$ means the transpose conjugate matrix, and $^{-1}$ means the inverse.

Thereby, following Cary (1998), $\hat{u}(\omega,p)$ can be considered the recorded wavefield in the $Tau$-$p$ domain, that is to say the incident wavefield times the corresponding free surface response coefficient for the slowness $p_j$:

$$\hat{u}^{\chi}_{\varrho}(\omega,p_j) = \varrho(\omega,p_j)R^{\chi}_{\varrho}(p_j)$$

where $\chi$ is the receiver direction ($x$ or $z$), $\varrho$ is the incident wave ($P$ or $S$). It can be expressed in terms of space by the inverse $Tau$-$p$ transform, according to equation 4:

$$u_k = \sum_{j=1}^{n_p} e^{i\omega p_j x_k}\hat{u}_j = \sum_{j=1}^{n_p} e^{i\omega p_j x_k}\left[\varrho_i(\omega,p_j)R^{\chi}_{\varrho}(p_j)\right] = u^{\chi}_{\varrho}(\omega,x_k) \quad ,$$

which can be represented as:

$$u^{\chi}_{\varrho}(\omega,x_k) = \sum_{j=1}^{n_p}\mathcal{B}^{\chi}_{\varrho}(p_j)\varrho(\omega,p_j) \quad .$$

Therefore the complete equations read:

$$\begin{pmatrix} u^Z(\omega,\vec{x}) \\ u^X(\omega,\vec{x}) \end{pmatrix} = \begin{pmatrix} \underset{\sim}{\mathcal{B}}^z_P(\omega,\vec{p},\vec{x}) & \underset{\sim}{\mathcal{B}}^z_S(\omega,\vec{p},\vec{x}) \\ \underset{\sim}{\mathcal{B}}^x_P(\omega,\vec{p},\vec{x}) & \underset{\sim}{\mathcal{B}}^x_S(\omega,\vec{p},\vec{x}) \end{pmatrix}\begin{pmatrix} P_i(\omega,\vec{p}) \\ S_i(\omega,\vec{p}) \end{pmatrix}$$

or

$$\begin{pmatrix} u^Z(\omega,\vec{x}) \\ u^X(\omega,\vec{x}) \end{pmatrix} = \underset{\sim}{\mathcal{B}}(\omega,\vec{p},\vec{x})\begin{pmatrix} P_i(\omega,\vec{p}) \\ S_i(\omega,\vec{p}) \end{pmatrix}$$

which enables us to obtain the incident $P$ and $S$ waves by using the least squares inversion algorithm as follows:

$$\begin{pmatrix} P_i(\omega,\vec{p}) \\ S_i(\omega,\vec{p}) \end{pmatrix} = \left(\underset{\sim}{\mathcal{B}}(\omega,\vec{p},\vec{x})^H \underset{\sim}{\mathcal{B}}(\omega,\vec{p},\vec{x})\right)^{-1} \underset{\sim}{\mathcal{B}}(\omega,\vec{p},\vec{x})^H \begin{pmatrix} u^Z(\omega,\vec{x}) \\ u^X(\omega,\vec{x}) \end{pmatrix} \tag{6}$$

These equations allow us to find the incident $P_i$ and $S_i$-waves from the recorded vertical and horizontal components, if the near surface velocities are known.

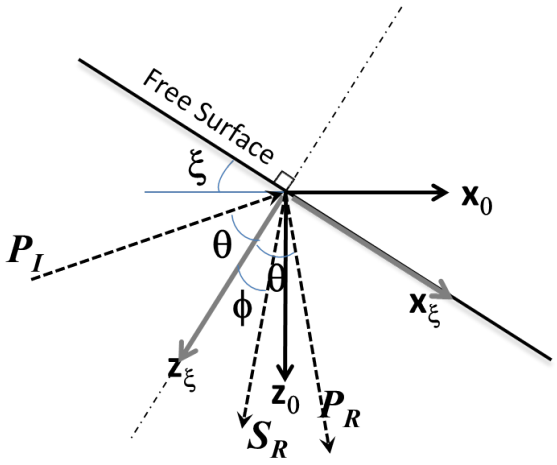


FIG. 3. Analysis of $P$-wave arriving at a sloping surface. Two coordinate axes are defined, $x_0$-$z_0$ corresponding to the horizontal and vertical directions, and $x_\xi$-$z_\xi$ to the directions parallel and normal to the surface. $P_I$ corresponds to the incident $P$âĂŞwave, $P_R$ to the reflected $P$-wave, and $S_R$ to the reflected S-wave.

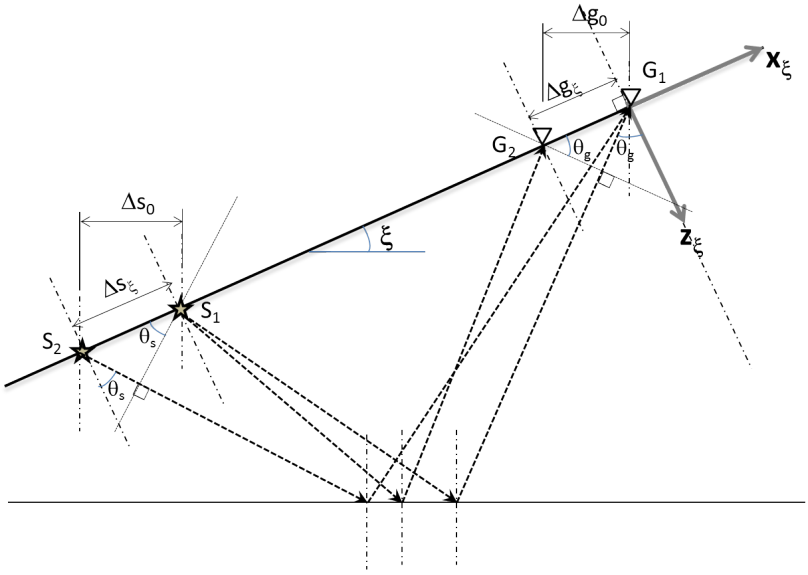


FIG. 4. Angles of incidence for $PS$-wave and their relation with the horizontal slowness $p$.

*Mode separation in rough terrain*

The sloping surface seismic wave recording is illustrated in Fig. 3, with an incident $P$-wave. The recording components are vertical and horizontal, but the normal to the surface

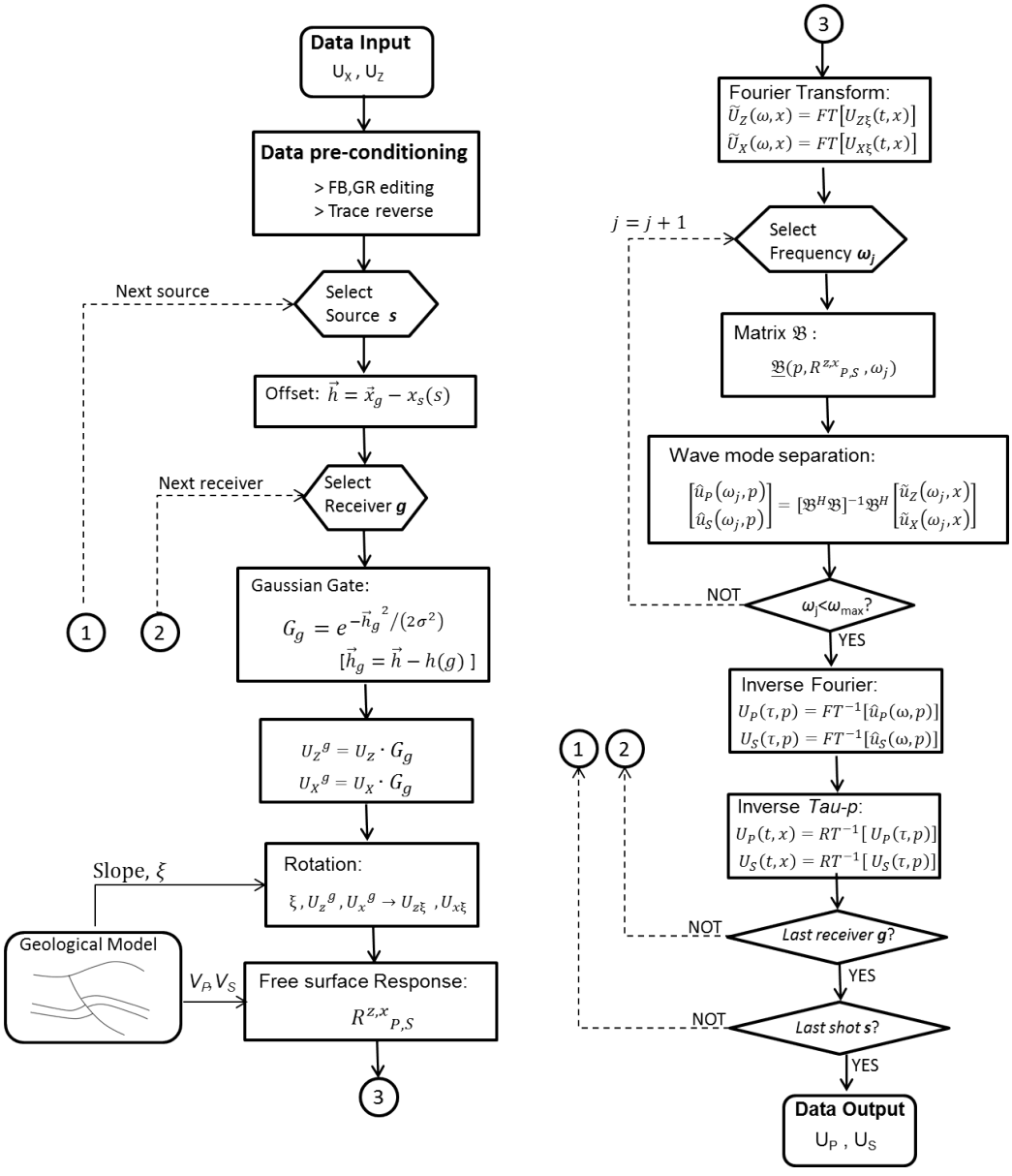


FIG. 5. Flow chart illustrating the complex area wave-mode separation method.

has an angle $\xi$ with the vertical. Therefore, a coordinate rotation is required to apply the method described above.

Figure 3 shows the coordinate system $x_0$-$z_0$, that corresponds to the vertical and horizontal directions, namely the recording component directions. The horizontal coordinate axis $x_0$ increases left to right and the vertical one $z_0$ is increases downward. The receiver location is assumed as the origin of the coordinate axes. The slope angle is $\xi$, and the rotated coordinate system is $x_\xi$-$z_\xi$. $P_I$ corresponds to the incident $P$ wave, $P_R$ to the reflected $P$-wave, and $S_R$ to the reflected $S$-wave. The relations between the recorded components on the vertical and horizontal axes and on the axes normal and parallel to the surface are:

$$u_{z\xi} = u_{z0}\ \cos\xi - u_{x0}\ \sin\xi \tag{7a}$$

$$u_{x\xi} = u_{z0}\ \sin\xi + u_{x0}\ \cos\xi \tag{7b}$$

These equations allow us to rotate the data recorded in the vertical and horizontal directions, after which the free surface coefficients method (equation 6) can be applied.

In the method discussed previously, the $p$ values amount to angles of incidence at the receiver (Figure 3), according to equation

$$p = \frac{\sin\theta}{V} = \frac{\Delta t}{\Delta x} \tag{8}$$

Figure 4 is a sketch of $PS$-wave arrival on a sloping free surface to compare source gather (CSG) and receiver gather (CRG) to select the right $p$ in the $Tau$-$p$ transform. $G_1$ is the receiver location to analyze. For a CRG, the $Tau$-$p$ transform would use the $\Delta t$ between two traces, namely the traces corresponding to sources $S_2$ and $S_1$. However this $\Delta t$ corresponds to the angle $\theta_s$. On the other hand, the $\Delta t$ between receivers $G_1$ and $G_2$, from the CSG of source $S_1$ corresponds to the receiver angle $\theta_g$, hence it is the appropriate domain to carry out the $Tau$-$p$ transform.

On the other hand, the analysis must be local to the receiver since the properties can change at each location, as has been discussed previously. A local $Tau$-$p$ transform (Milkereit, 1987) is a tradeoff for the requirement of local analysis and the $Tau$-$p$ integral character. It is defined as:

$$u_0(\tau, p) = \int_{x_0-\delta}^{x_0+\delta} u(\tau + px, x) W(x_0 - x) \mathrm{d}x$$

where $u(t, x)$ is a seismic data record in time and space, $x_0$ is the reference location, and $W(x_0 - x)$ is a weight function that depends on the distance to the reference location. Regarding the weight function $W(x_0 - x)$, a *Gaussian* function appears to be an appropriate option taking into account its properties (Margrave et al., 2011), namely that it is a smooth function, that the weight decreases with distance and that allows the reconstruction of a piecewise signal. It is defined by the following equation:

$$W(x_0 - x) = a \exp\left(\frac{-(x_0 - x)^2}{2\sigma^2}\right) \tag{9}$$

where $a$ is the peak value, which is assumed one for our purpose, $x_0$ is the position of the center of the peak, $x$ are the positions of the other points, and $\sigma$ defines the shape of the Gaussian with respect to the peak value, which corresponds to the *standard deviation* of the Gaussian function.

The wave mode separation method for rough terrain just described in the previous paragraphs, is illustrated by the flow chart of Figure 5.

## Multicomponent migration with topography

Two preSDM methods were applied, Kirchhoff and Phase Shift plus Interpolation or PSPI. Each one of them utilizes a different approach, namely Kirchhoff is non-recursive and is based on an integral solution to the wave equation, whereas PSPI is recursive (or depth-continuation type) and is based on a differential solution (Gray et al., 2001). These methods are applied using the shot-profile scheme, which can help avoid aliasing in complex areas, where source sampling is typically coarser and more irregular than receiver sampling (Biondi, 2006). As illustrated below, two stages can be identified in the migration process: *wave extrapolation* and *imaging condition*.

### *Kirchhoff method*

The theoretical model is derived from the Green's Theorem that relates a vector field in the interior of a volume with the same field on the surface (Shearer, 1999). The Kirchhoff equation results, e.g the shape presented by Wiggins (1984):

$$U_1(\vec{x_1}, t) = \frac{-1}{v} \int_{S_0} \frac{1}{r} \frac{\partial r}{\partial n} \left[ \frac{\partial U_0}{\partial t} \left( \vec{x_0}, t + \frac{r}{c} \right) \right] \mathrm{d}S_0 \tag{10}$$

which is a function that allows us to obtain the wavefield at a point in the interior of a surface $U_1(\vec{x_1}, t)$ , as a function of the measurements on the surface $U_0(\vec{x_0}, t)$ (see e.g. Shearer, 1999; Wiggins, 1984). Therefore it is an extrapolation equation, which can be used for many purposes. Together with the *imaging condition* it becomes a migration method, such as the following equation applied to zero offset migration with a flat surface:

$$U_1(x_1, y_1, z_1, t = 0) = \frac{1}{2\pi} \int \int_{S_0} \frac{1}{rv/2} \cos\theta \left[ \frac{\partial U_0}{\partial t} \left( x, y, z = 0, t = \frac{r}{v/2} \right) \right] \mathrm{d}x\mathrm{d}y$$

where

$$r = \left[ (x_1 - x)^2 + (y_1 - y)^2 + z_1^2 \right]^{1/2}$$

$\theta$ is the angle between the $z$ axis and the line joining $U_0$ and $U_1$, and $t$ is the two way travel time (Margrave, 2007).

Following Biondi (2006), the Kirchhoff method of shot-profile prestack migration in 2-D, for a point inside the media located at $x_\varepsilon$, $z_\varepsilon$, can be represented in a generalized form as:

$$I_s(\vec{x_\varepsilon}) = \int_\Sigma W(\vec{x_\varepsilon}, \vec{x_s}, \vec{x_g}) U[t = t(\vec{x_\varepsilon}, \vec{x_s}, \vec{x_g}), \vec{x_s}, \vec{x_g}] \, \mathrm{d}x_g \tag{11}$$

where $\vec{x_\varepsilon} = (x_\varepsilon, z_\varepsilon)$, $W(\vec{x_\varepsilon}, \vec{x_s}, \vec{x_g})$ represents the amplitude weight correction obtained according to the Kirchhoff theory, $U[t, \vec{x_s}, \vec{x_g}]$ the input wavefield with source at $\vec{x_s}$ and receiver at $\vec{x_g}$ (a shot gather in this case), $I_s(\vec{x_\varepsilon})$ is the migrated image, $\Sigma$ is the *migration aperture*, and $t(\vec{x_\varepsilon}, \vec{x_s}, \vec{x_g})$ is the two-way travel time between the surface locations and the point inside the medium.

PreSDM for $PP$ and $PS$ waves with topography can be represented by equation 11. The time $t(\vec{x_\varepsilon}, \vec{x_s}, \vec{x_g})$ is obtained from a forward modeling method, such as ray tracing, over a velocity model provided previously. In the case of $PS$-waves it requires a velocity model for $P$ wave at the source side and for $S$ wave at the receiver side. Figure 6 shows the flow chart for Kirchhoff multicomponent PreSDM from topography*.

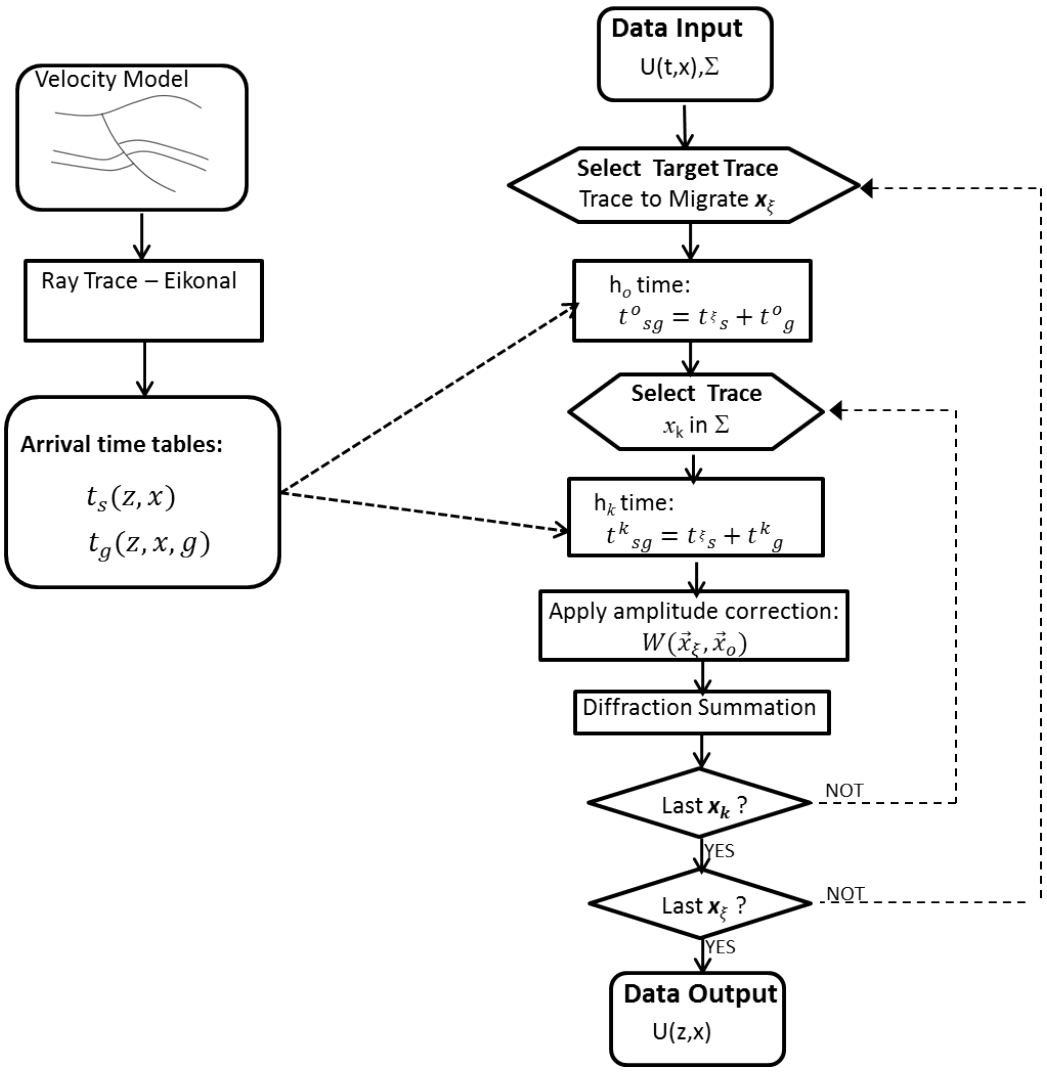


FIG. 6. Flow chart for Kirchhoff multicomponent PreSDM with topography.

*The code is included into the CREWES migration tools, under kirk_shotcz.m

*PSPI method*

The 2-D scalar wave equation after the Fourier transform in the coordinates $x$ and $t$, that is as a function $\tilde{\tilde{U}}(k_x, \omega, z)$ , can be separated into two one-way wave equations. The down-going wave is

$$\frac{\partial \tilde{\tilde{U}}(k_x, z, \omega)}{\partial z} = ik_z \tilde{\tilde{U}}(k_x, z, \omega) = 0 \quad , \tag{12}$$

where

$$k_z = \frac{\omega}{v}\sqrt{1 - \left(\frac{k_x v}{\omega}\right)^2} \quad .$$

Equation 12 has the solution

$$\tilde{\tilde{U}}_{z+\Delta z}(\omega, k_x) = \tilde{\tilde{U}}_z(\omega, k_x) e^{(ik_z \Delta z)} \quad , \tag{13}$$

which can be verified by substitution. This is the *Phase shift* extrapolation equation.

The migration method based on this approach is known as *Phase-Shift migration*. However it cannot handle lateral velocity variations. A method known as *Phase Shift plus Interpolation*, shortened to *PSPI*, was proposed to overcome this shortcoming (Gazdag and Sguazzero, 1984). Basically a number of Phase-shift migrations, each one with a different velocity corresponding to lateral variation, is carried out, and the results are interpolated.

Additional proficiency was provided by the work of Margrave and Ferguson (1999) and others, that allows more continuous variation of the velocity in $x$ (see also Bale, 2006). The preSDM method used in this work is based on this approach, according to Al-Saleh et al. (2009). * . The extrapolation equation (backward propagation) for the upgoing wavefield $\tilde{U}(x, \omega)$, according to Al-Saleh (2006), is:

$$\tilde{U}_{n\Delta z}(x, \omega) = \frac{1}{2\pi} \int \int_{-\infty}^{\infty} \tilde{U}_{(n-1)\Delta z}(x', \omega) e^{-ik_x x'} \, \mathrm{d}x' e^{i\sqrt{k_n^2 - k_x^2}\Delta z} e^{-ik_x x} \, \mathrm{d}k_x$$

where $\Delta z$ is the depth step size, $n$ is the number of the depth step, $\omega$ is the temporal frequency, $k_x$ is the wavenumber in the direction $x$, and $k_n$ is the magnitude of the wavenumber vector at $n$. An analogous expression can be defined for the downgoing wavefield, namely the source:

$$\tilde{D}_{n\Delta z}(x, \omega) = \frac{1}{2\pi} \int \int_{-\infty}^{\infty} \tilde{D}_{(n-1)+\Delta z}(x', \omega) e^{-ik_x x'} \, \mathrm{d}x' e^{-i\sqrt{k_n^2 - k_x^2}\Delta z} e^{-ik_x x} \, \mathrm{d}k_x$$

The source implemented for this code is a numerical evaluation of the free-space Green's function $G_0$ at the first depth level below the source, which is a better representation than the extrapolation of a unit pulse, as shown by Al-Saleh et al. (2009). For 2-D it is expressed using a Hankel function of the first kind $H_0^{(1)}$ (see Al-Saleh et al., 2009).

*The code is included into the CREWES migration tools, under pspi_shot_cwavez.m

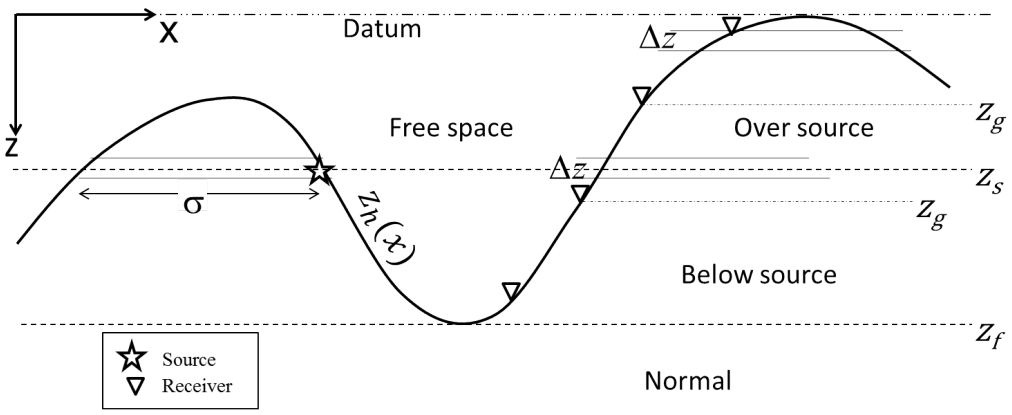


FIG. 7. Illustration of the space domain types in the PSPI migration from topography algorithm.

The deconvolution imaging condition, following Al-Saleh (2006) is:

$$I(x,z) = \int_{\omega_i}^{\omega_f} \frac{U(x,z,\omega)D^*(x,z,\omega)}{D(x,z;\omega)D^*(x,z,\omega) + \mu I_{max}(z)} \mathrm{d}\omega \tag{14}$$

where the asterisk $(*)$ means conjugate, and $\mu I_{max}(z)$ is a stabilizing factor. The integral on $\omega$ amounts for the $t = 0$ corresponding to the imaging condition.

This approach allows preSDM from topography, as shown by Al-Saleh et al. (2009). The relevant properties of topography are illustrated in Figure 7. The surface elevation as a function of the horizontal coordinate is represented by $z_h(x)$. The receiver elevations are $z_g$, the source elevation is $z_s$, and the lowest elevation is $z_f$. The flow chart of Figure 8 illustrates the migration procedure.

The extrapolation below $z_f$ is just the usual for a flat surface. It is represented by the function $\Phi$. Above it we define the *topography zone*, where the extrapolation depends on the location of the current elevation $z_j$ compared with the source location $z_s$. The extrapolation in the topography zone is represented by the function $\Phi_z$, which is described in figure 9. It allows the variation of properties in the horizontal direction $x$, since at the same level it is possible to have locations inside of the terrain, on the surface, or above the surface, which define what kind of extrapolation is required.

## APPLICATION TO SYNTHETIC DATA

These methods were tested on a synthetic data set. In the following firstly it is described the data set, then wave mode separation application is presented and finally the migration methods are introduced.

### Synthetic data generation

The geological model used to generate these data is illustrated in figure 10. Its dimensions are 1000 m horizontal and 1000 m vertical. It includes characteristics such as rough topography, represented by a hill with a slope of $16^\circ$ and a height of 135 m above the ground plane, and a complex geological structure, with a fault with $65^\circ$ slope and a dipping

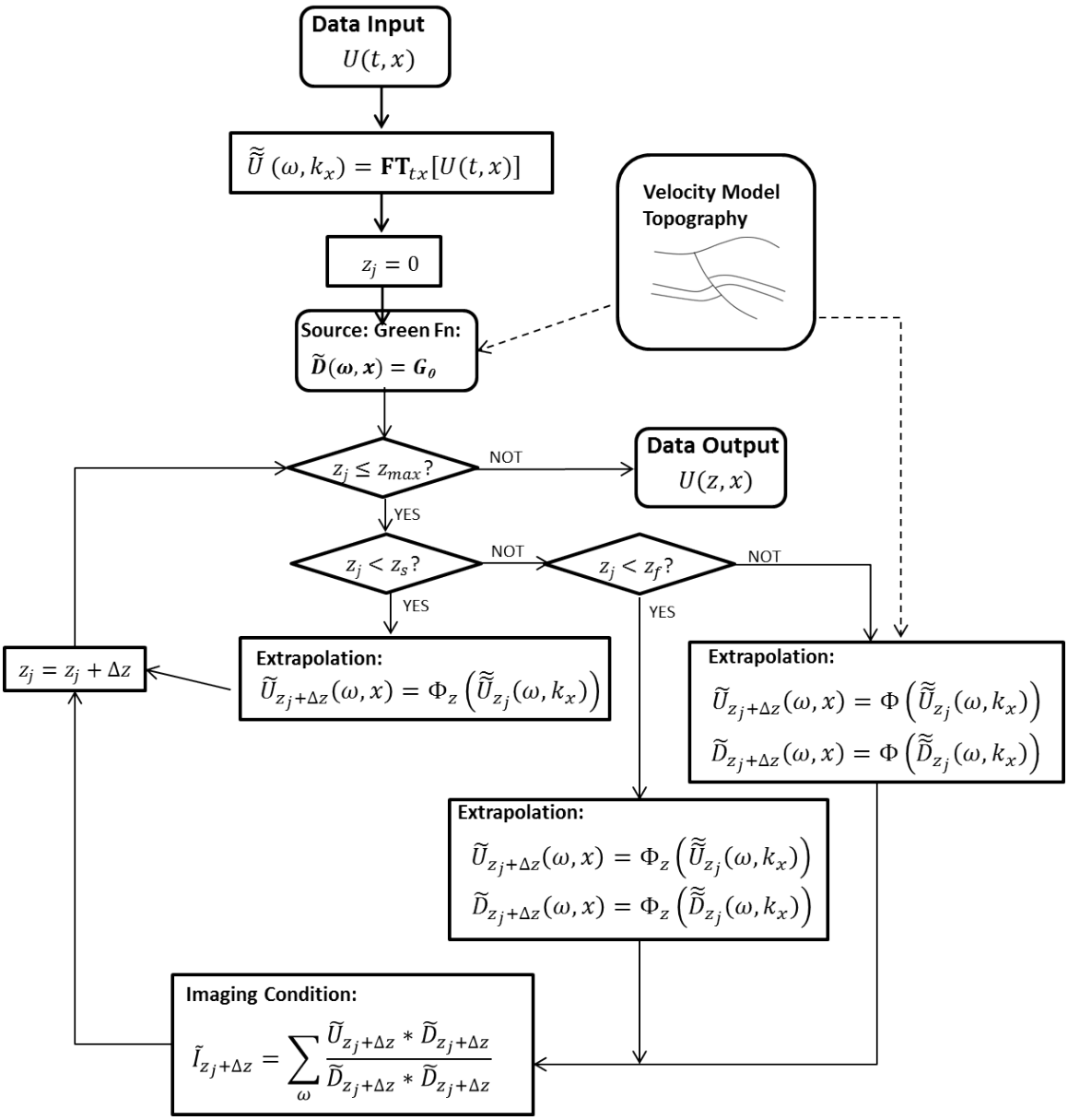


FIG. 8. Flow diagram for prestack PSPI migration with topography.The depths $z_s$,$z_g$, and $z_{tm}$ are illustrated in figure 7. The extrapolation function $\Phi_z$ is explained in figure 9.

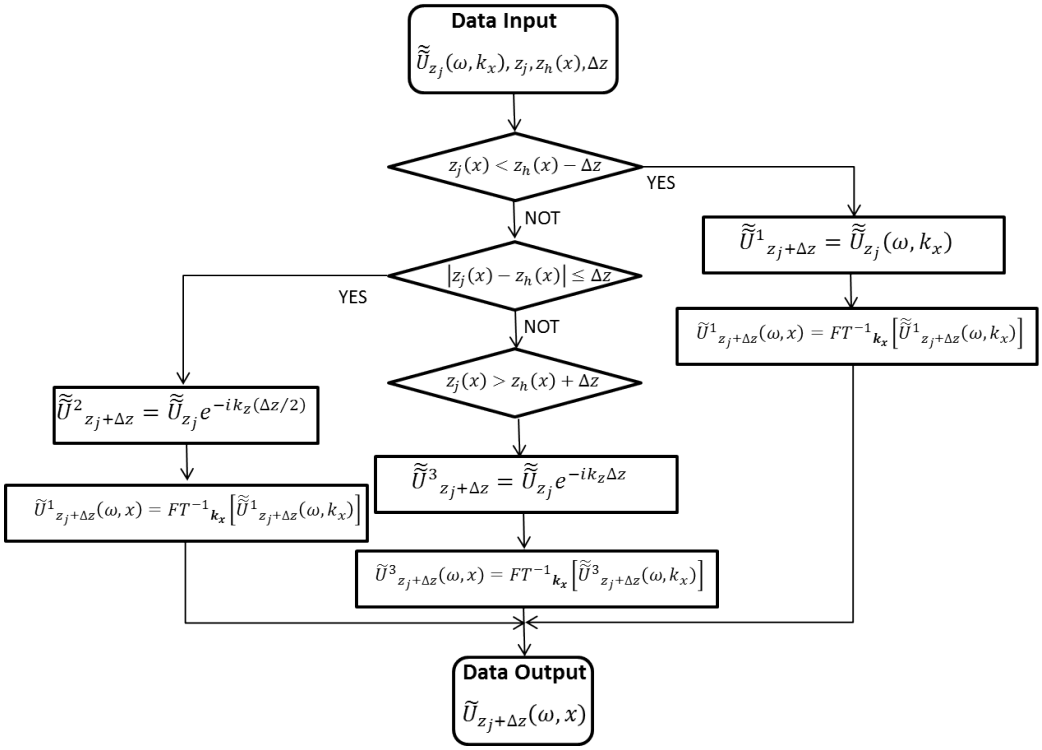


FIG. 9. Flow chart of the function $\Phi_z$ that carries out the phase-shift extrapolation with topography.

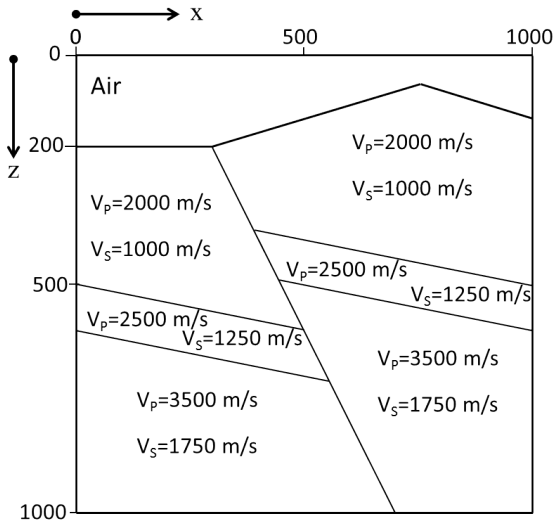


FIG. 10. Geological model with topography and structure to test the PreSDM methods. The left and right hand sides are separated by an inverse fault. The surface shows a hill with 135 m high. The target is the dipping layer.

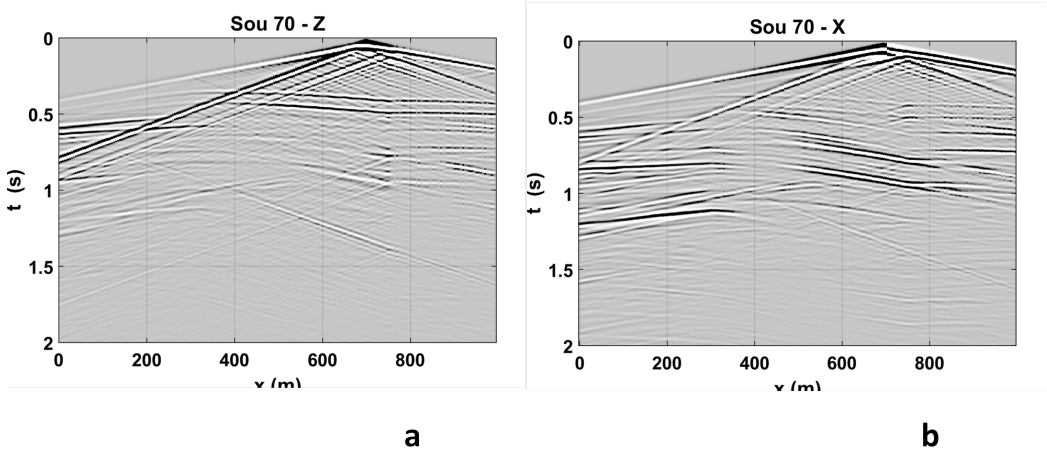


FIG. 11. An example of the synthetic records obtained with elastic FD difference modeling, corresponding to shot 70 (x=700 m). (a) Vertical component (b) horizontal component.

layer with about $12^\circ$ slope, which is assumed to be the imaging target. The velocities of this layer are $V_P$ of 2500 m/s and $V_S$ 1250 m/s.

The synthetic data were generated with the Finite difference (FD) method, using a 2D, elastic, isotropic algorithm, following Hayashi et al. (2001), which allows implementing an irregular surface. Forty one shots were generated, from the location $x = 100$ m to $x = 900$ m, separated by 20 m. The receivers are on the free surface, separated by 5 m, for a total of 200. Time sampling is 2 ms, and the record length is 2 s. The source is a symmetrical Ricker wavelet with a center frequency of 20 Hz and a length of 100 ms, starting at zero time.

Figure 11 shows an example of one of the resulting shot gathers, whose source is located at $x$ 700 m. Figure 11a corresponds to the vertical component and figure 11b to the horizontal component. Many events can be observed on both records, principally $P$-waves on the vertical component and $S$-waves on the horizontal, as usually assumed.

*Wave mode separation*

The wave mode separation method proposed above (Figure 5) was applied to the synthetic data just described. The Gaussian gate (equation 9) was applied to the input with standard deviation $\sigma$ of 30 m, equivalent to six receiver locations.

The result is illustrated by Figure 13, corresponding to the shot gathers of Figure 11. Figure 13a corresponds to the $P$-wave and Figure 13b to the $S$-wave. Arrival times calculated with ray-tracing (using the software Norsar-2D) show up in Figure 12, over low gain records, namely $P$-wave arrivals in Figure 12a and $S$-wave arrivals in Figure 12b. Comparing with Figure 11, it can be noticed that some of the events identified as leakage, namely energy of the alternate wave mode, $P$-waves in the horizontal component and $S$-waves in the vertical component, have been attenuated in Figure 13, and events properly identified as the corresponding wave-mode by ray tracing appear stronger after wave mode separation. However some of the leakage energy is still present, specially in the right-hand side.

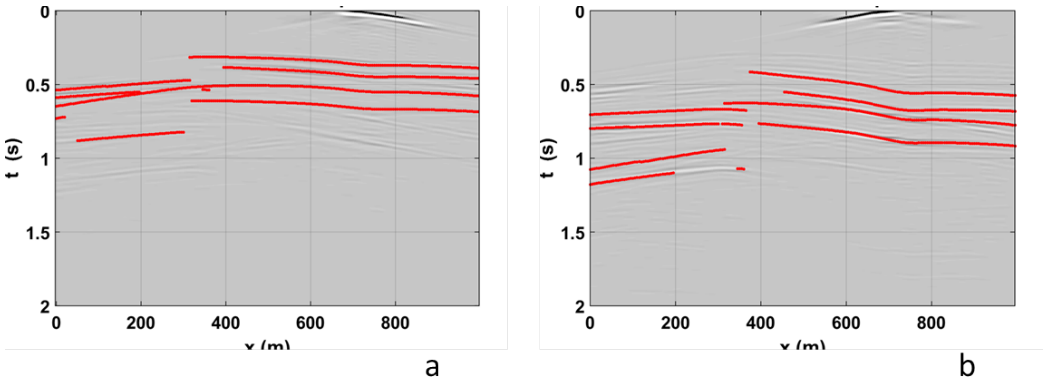


FIG. 12. Arrival times obtained by ray-tracing for the synthetic record shot 70 (x=700 m) on a low gain seismic record. (a) $P$-waves (b) $S$-waves.

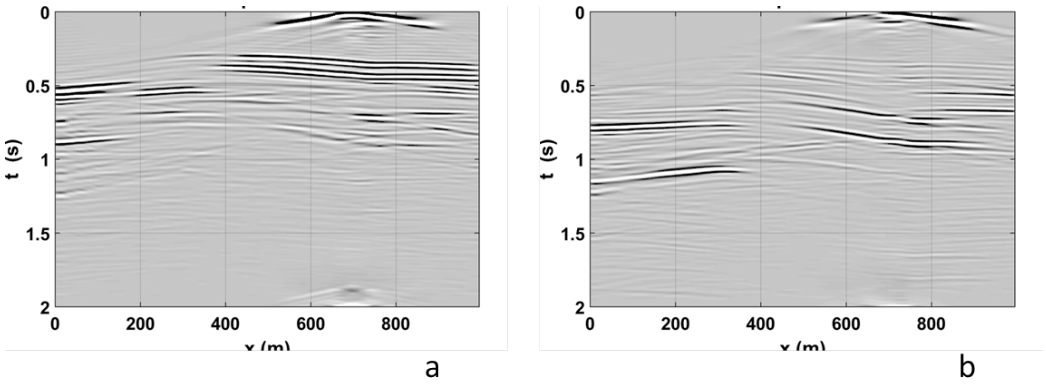


FIG. 13. Seismic events after wave mode separation for the synthetic gather corresponding to shot 70 (x=700 m). (a) $P$-waves (b) $S$-waves. Notice that leakage events (compare with Figures 11 and 12) have been attenuated specially at the far offsets, however other remain.

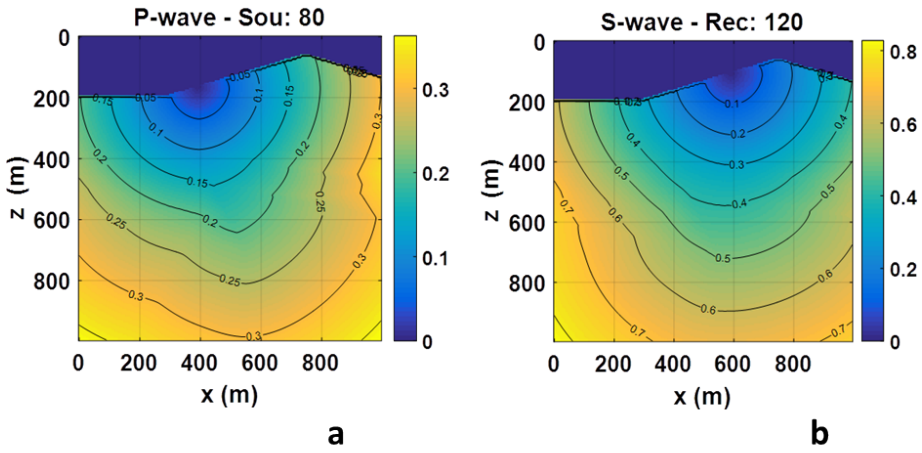


FIG. 14. Arrival times table examples for Kirchhoff migration (a) $P$-wave shot at x=400 m (b) $S$-wave, receiver at x=600 m.

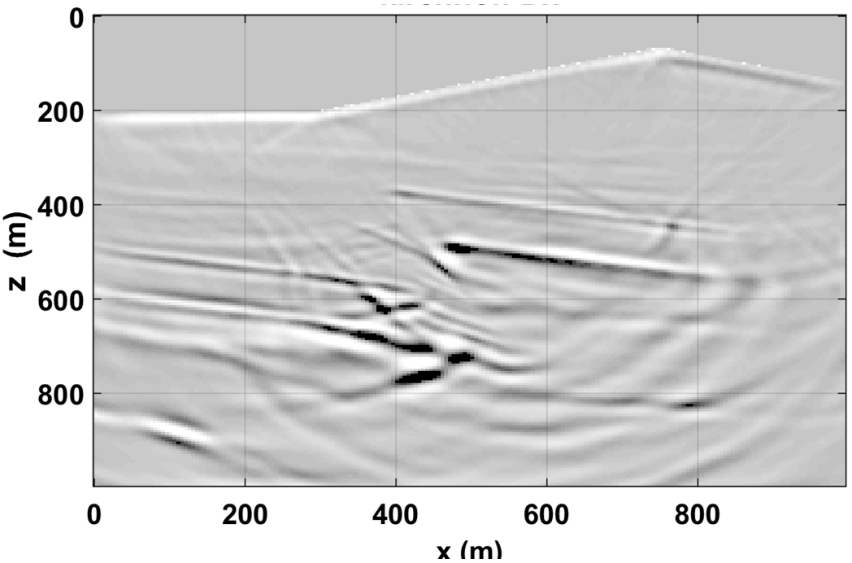


FIG. 15. Kirchhoff PreSDM for the $PS$-wave using the horizontal component, without wave mode separation.

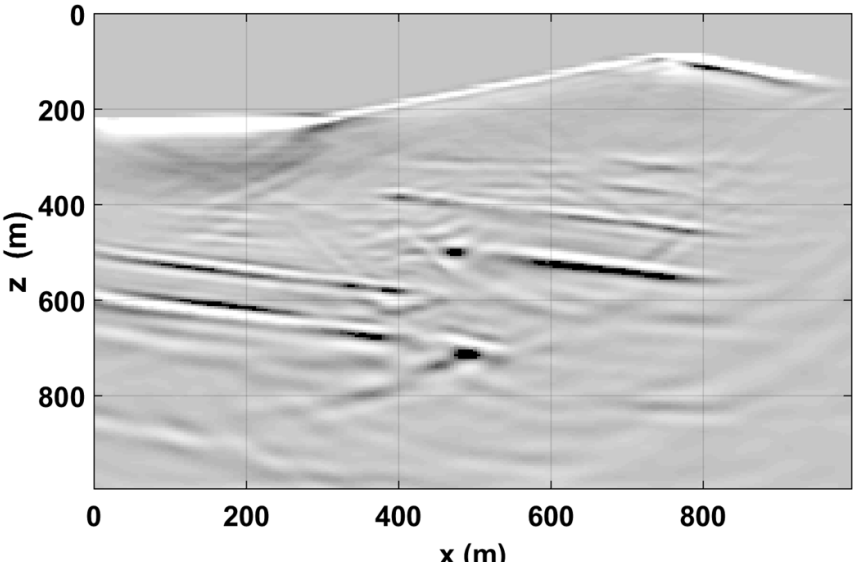


FIG. 16. Kirchhoff PreSDM for the $PS$-wave after wave mode separation.

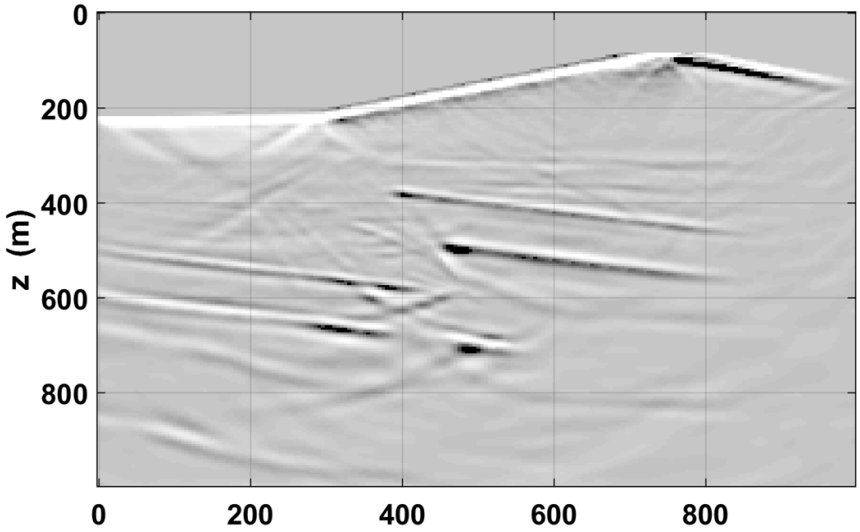


FIG. 17. PSPI PreSDM for the $PS$-wave using the horizontal component, without wave mode separation.

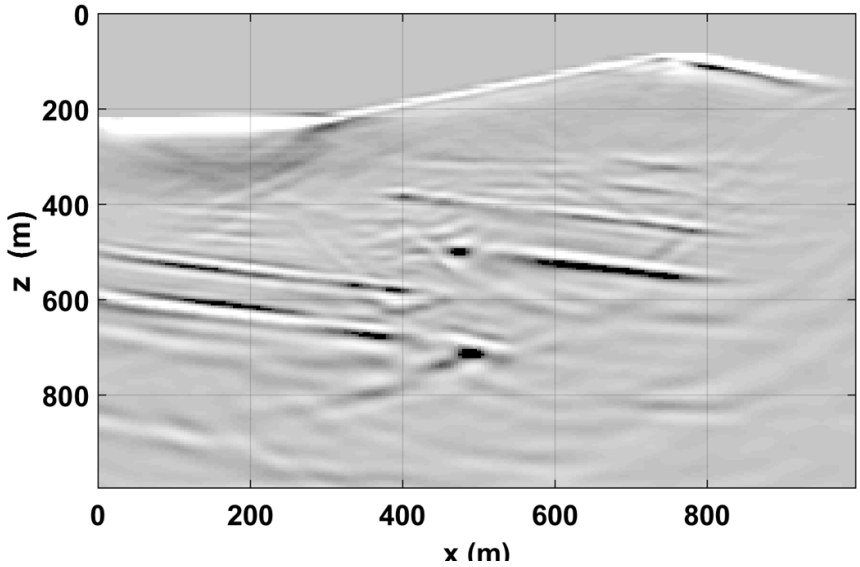


FIG. 18. PSPI PreSDM for the $PS$-wave after wave mode separation.

*Kirchhoff migration*

Figure 14 illustrates the arrival times calculated with an eikonal equation software[‡], corresponding to the $P$-wave (source side) in Figure 14a and to the $S$-wave (receiver side) in Figure 14b. Figures 15 and 16 illustrate the results of Kirchhoff migration for the $PS$-wave, without and with wave mode separation. The depth location of the events agree with the original geological model (Figure 10). After wave mode separation subtle differences in amplitude can be noticed. Strong artifacts are present in both cases, which can be attributed partially to the shortcomings of the algorithm when applied to complex areas (Gray et al., 2001) and to $PS$ waves.

*PSPI migration*

Figure 17 shows the resulting migrated $PS$ data using the PSPI method without wave mode separation. Figure 18 is the result after wave mode separation. The depths of events also correspond closely to the expected depths in the geological model. However similarity to the Kirchhoff migration in the previous section should be noted; there is just a subtle difference, such that the benefit of wave mode separation is not apparent.

## DISCUSSION

Previous work using a wave-mode separation method for a sloping free surface with the same approach, presented in Guevara et al. (2013), shows the expected separated $P$ and $S$-waves. There are significant differences between that experiment and the example presented here, such as:

- A more complex (but realistic) wavefield, was used in this work, since modeling was carried out using FD, while in the previous work it was used ray tracing, which leads to a more simplified wavefield.
- The deep geological model used in the earlier results did not included any structure, but a flat reflector, compared with the complex model this time (Figure 10).
- The surface of the earlier model had a constant slope, compared with the hill shape used in this case.

The wave mode separation in this work appears effective up to a point (Figure 13). However the benefit of wave mode separation is not apparent in the data after preSDM. Migration algorithms have shortcomings that have been discussed in the literature (e.g. Biondi, 2006; Gray et al., 2001). However the result can also be attributed to shortcomings of the mode separation method for such a complex problem. As an example, taking into account the short-distance variation in properties, a local $Tau$-$p$ transform was applied, however it can introduce boundary artifacts. On the other hand the complex wavefield can overcome the assumptions of the method, namely waves can arrive with an angle that perhaps the $Tau$-$p$ transform cannot find out with appropriate accuracy.

[‡]The eikonal code used is in the CREWES tools, called eikonal2d.m

## CONCLUSIONS

- We propose a method for wave mode separation for a complex setting, based on the approach of Dankbaar (1985), taking into account the free surface response and the topography. It requires the velocities for $P$ and $S$-waves and the slope at the near surface receiver location.
- A local $Tau$-$p$ transform has been applied on the CSG domain, to obtain the required plane wave decomposition at each receiver location. It appears appropriate assuming that the relevant properties typically can change for each receiver.
- The example, from a complex model and using FD modeling, shows reasonable resulting wave mode separation, even though with residual leakage. However the migration results are not as rewarding as expected, which could be attributed partially to little free surface effect and/or migration shortcomings, besides that the method itself.
- Both depth migration methods from the topography gave correct reflector depths, and show the same structure, however with the presence of artifacts, partially attributable to the migration algorithms.
- The method deserves additional analysis, such as to identify limitations in the theoretical model or the $Tau$-$p$ transform application.
- The potential of the wave separation method for such a challenging environment can be defined with additional more extended test, since it shows partial success. For the current techology, linking $P$-wave with the vertical component and $S$-wave with the horizontal appears good enough in most cases.

## ACKNOWLEDGEMENTS

The financial support of the CREWES sponsors contributed to carry out this work. The technical support of CREWES staff was instrumental in the generation and testing of the computer codes, and in the writing of this report. We also thank Ecopetrol who provided the modeling software to generate the synthetic data.

## REFERENCES

Al-Saleh, S. M., 2006, Designing explicit wavefield extrapolators for depth migration and migration velocity analysi: Ph.D. thesis, Univ. of Calgary.

Al-Saleh, S. M., Margrave, G. F., and Gray, S. H., 2009, Direct downward continuation from topography using explicit wavefield extrapolation: Geophysics, **74**, S105–S112.

Bale, R. A., 2006, Elastic wave-equation depth migration of seismic data for isotropic and azimuthally anisotropic media: Ph.D. thesis, Univ. of Calgary.

Biondi, B., 2006, 3D seismic imaging: SEG Investigations in Geophysics No. 14.

Cary, P. W., 1998, P/S wavefield separation in the presence of statics: CREWES Reseach Report, **10**, 30.1–30.8.

Dankbaar, J. W. M., 1985, Separation of P- and S-waves: Geophysical Prospecting, **33**, 970–986.

Donati, M. S., 1996, P- and S- wave separation using three-component modal filters: M.Sc. thesis, University of Calgary.

Gazdag, J., and Sguazzero, P., 1984, Migration of seismic data by phase shift plus interpolation: Geophysics, **49**, 124–131.

Gray, S. H., Etgen, J., Dellinger, J., and Whitmore, D., 2001, Seismic migration problemas and solutions: Geophysics, **66**, 1622–1640.

Gray, S. H., and Marfurt, K. J., 1995, Migration from topography: improving the near surface image: Canadian Journal of Exploration Geophysics, **31**, 18–24.

Guevara, S. E., and Margrave, G. F., 2011, Converted wave prestack depth migration from topography: a comparison: CREWES Research Report, **23**, 34.1–34.12.

Guevara, S. E., Margrave, G. F., and Lawton, D. C., 2013, Wave mode separation for a surface with slope using the free-surface response: CREWES Research Report, **25**, 29.1–29.6.

Hayashi, K., Burns, D. R., and Toksoz, M. N., 2001, Discontinuous-grid finite-difference seismic modeling including surface topography: Bull. Seism. Soc. of America, **91**, 1750–1764.

Marfurt, K. J., Schneider, R. V., and Mueller, M. C., 1996, Pitfalls of using conventional and discrete radon transforms on poorly sampled data: Bull. Seism. Soc. of America, **91**, 1750–1764.

Margrave, G. F., 2007, Methods of seismic data processing: University of Calgary: course lecture notes.

Margrave, G. F., and Ferguson, R. J., 1999, Wavefield extrapolation by non-stationary phase shift: Geophysics, **64**, 1067–1078.

Margrave, G. F., Lamoureux, M. P., and Henley, D. C., 2011, Gabor deconvolution: estimating reflectivity by nonstationary deconvolution of seismic data: Geophysics, **76**, W15–W30.

Meissner, R., 1965, P- and SV- waves from uphole shooting: Geophysical Prospecting, **13**, 433–459.

Milkereit, B., 1987, Decomposition and inversion of seismic data - an instantaeous slowness approach: Geophysical Prospecting, **35**, 875–894.

Shearer, P. M., 1999, Introduction to seismology: Cambridge University Press.

Van der Baan, M., 2006, PP/PS wavefield separation by independent component analysis: Geophys. J. Int., **166**, 339–348.

Wiggins, J. W., 1984, Kirchhoff integral extrapolation and migration of nonplanar data: Geophysics, **49**, 1239–1248.